Journal of
Synchrotron
Radiation

ISSN 1600-5775

Received 27 January 2014
Accepted 27 May 2014

FemtoSpeX: a versatile optical pump–soft X-ray probe facility with 100 fs X-ray pulses of variable polarization

Karsten Holldack,[a]* Johannes Bahrdt,[a] Andreas Balzer,[a] Uwe Bovensiepen,[b] Maria Brzhezinskaya,[a] Alexei Erko,[a] Andrea Eschenlohr,[b] Rolf Follath,[a,c] Alexander Firsov,[a] Winfried Frentrup,[a] Loïc Le Guyader,[a] Torsten Kachel,[a] Peter Kuske,[a] Rolf Mitzner,[a] Roland Müller,[a] Niko Pontius,[a] Torsten Quast,[a] Ilie Radu,[a] Jan-Simon Schmidt,[a] Christian Schüßler-Langeheine,[d] Mike Sperling,[a] Christian Stamm,[e,a] Christoph Trabant[d,a]‡ and Alexander Föhlisch[a]¶

[a]Helmholtz-Zentrum Berlin für Materialien und Energie, Albert-Einstein-Strasse 15, Berlin 12489, Germany, [b]Fakultät für Physik, Universität Duisburg-Essen, Lotharstrasse 1, Duisburg 47048, Germany, [c]SLS, Paul Scherrer Institut, Villigen 5232, Switzerland, [d]II. Physikalisches Institut, Universität zu Köln, Zülpicher Strasse 77, Köln 50937, Germany, and [e]Department of Materials, ETH Zürich, Zürich CH-8093, Switzerland. *E-mail: karsten.holldack@helmholtz-berlin.de

Here the major upgrades of the femtoslicing facility at BESSY II (Khan *et al.*, 2006) are reviewed, giving a tutorial on how elliptical-polarized ultrashort soft X-ray pulses from electron storage rings are generated at high repetition rates. Employing a 6 kHz femtosecond-laser system consisting of two amplifiers that are seeded by one Ti:Sa oscillator, the total average flux of photons of 100 fs duration (FWHM) has been increased by a factor of 120 to up to 10^6 photons s^{-1} (0.1% bandwidth)$^{-1}$ on the sample in the range from 250 to 1400 eV. Thanks to a new beamline design, a factor of 20 enhanced flux and improvements of the stability together with the top-up mode of the accelerator have been achieved. The previously unavoidable problem of increased picosecond-background at higher repetition rates, caused by 'halo' photons, has also been solved by hopping between different 'camshaft' bunches in a dedicated fill pattern ('3+1 camshaft fill') of the storage ring. In addition to an increased X-ray performance at variable (linear and elliptical) polarization, the sample excitation in pump–probe experiments has been considerably extended using an optical parametric amplifier that supports the range from the near-UV to the far-IR regime. Dedicated endstations covering ultrafast magnetism experiments based on time-resolved X-ray circular dichroism have been either upgraded or, in the case of time-resolved resonant soft X-ray diffraction and reflection, newly constructed and adapted to femtoslicing requirements. Experiments at low temperatures down to 6 K and magnetic fields up to 0.5 T are supported. The FemtoSpeX facility is now operated as a 24 h user facility enabling a new class of experiments in ultrafast magnetism and in the field of transient phenomena and phase transitions in solids.

Keywords: femtosecond X-ray pulses; storage ring; elliptical undulators; slicing; diffractive optics; time-resolved X-ray spectroscopy; ultrafast science.

1. Introduction

Variably polarized ultra-short synchrotron radiation pulses in the soft X-ray spectral range are optimal tools for exploring ultrafast phenomena in condensed matter (Stamm *et al.*, 2007; Gavrila *et al.*, 2009; Boeglin *et al.*, 2010; Holldack *et al.*, 2010). Laser-driven ultrafast magnetization dynamics on elementary length and timescales are of specific interest (Wietstruk *et al.*, 2011; Radu *et al.*, 2011; Eschenlohr *et al.*, 2013) to reveal ultimate speeds of magnetization reversal. Stable X-ray pulses of 100 fs duration and elliptical polarization are well suited to support these studies providing an 'ultimate view' on spin dynamics (Koopmanns, 2007).

Slicing facilities (Zholents & Zolotorev, 1996; Schoenlein *et al.*, 1996, 2000; Khan *et al.*, 2006; Ingold *et al.*, 2007) generate intrinsically synchronized femtosecond X-ray and femto-

‡ Now at Freie Universität Berlin, Germany.
¶ Also at Universität Potsdam, Germany.

second laser pulses, which is the most salient advantage of storage-ring-based sources compared with similar experiments at free-electron lasers (FELs) without seeding (Yu, 1991). Existing seeded FELs (FERMI, 2013) do not cover the X-ray energy range of interest yet. The simple fact that X-ray pulses generated by femtoslicing are always extracted from the same electron bunch results in a very low charge fluctuation and hence leads to constant intensity and high temporal stability of the X-ray probe pulses. This, together with the persistent demand for elliptically polarized photons, encouraged us to further upgrade femtoslicing at BESSY towards an ultrafast user facility complementary to FELs.

In 2010 we renamed the upgraded slicing facility to FemtoSpeX which is mainly a set-up to study ultrafast dynamics with soft X-ray pulses of ∼100 fs (FWHM) duration at photon energies from 250 to 1400 eV with variable elliptical polarization from an undulator according to the scheme shown in Fig. 1. As illustrated here, the energy modulation of electrons co-propagating with a laser pulse through a wiggler (U139) causes the emission of short-pulse elliptical radiation by a subsequent elliptical undulator UE56 of the APPLE II type, where elliptical light is produced by a shift of magnetic rows (Sasaki *et al.*, 1992; Bahrdt, 2012). Short-pulse undulator radiation from laser-energy modulated electrons occurs at different emission angles and points into the beamline while either the regular radiation or the short-pulse component is kicked into a dump. The user can decide to use regular X-ray pulses or 100 fs pulses (shaded red in Fig. 1), albeit at less flux, in a pump–probe experiment.

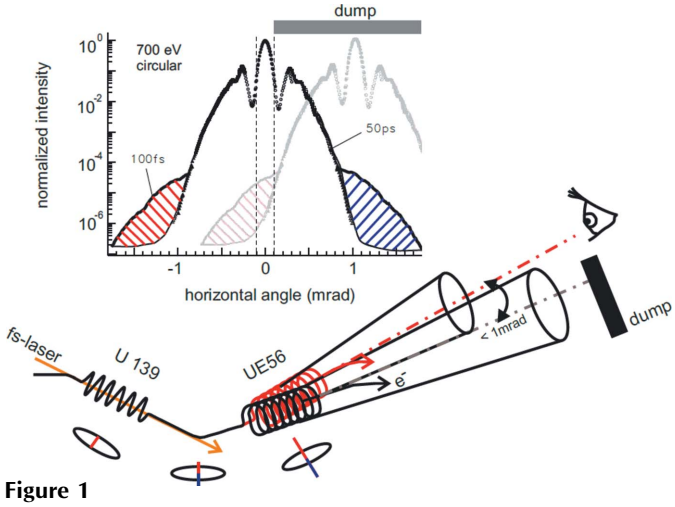

Figure 1
Principle of femtoslicing at BESSY II. After being laser-energy modulated in the planar wiggler (U139), electrons emit elliptically polarized soft X-ray pulses in the radiator UE56 after passing a deflecting dipole magnet. Regular electrons (black ellipse) and energy-modulated electrons in the 'slice' expect either energy loss (red bar) or energy gain (blue bar). After passing a magnet they emit short-pulse elliptically polarized synchrotron radiation in the UE56 under different emission angles of the order of 1 mrad. A local orbit bump in the electron beam path can be used on user's demand to point either X-rays of ∼50 ps or ∼100 fs duration into the beamline (eye). As indicated by the measured angular distribution in the inset taken at a photon energy of 700 eV, only the angular part from the loss electrons (red) is kicked into the beamline (acceptance marked by dashed lines) while all other photons, also from higher energetic electrons (blue), are sent into the dump.

Here we review all substantial upgrades of the facility that have considerably improved the performance within the past few years. These main improvements are: (i) increase of the repetition rate and solving the problems of its consequences; (ii) slicing under improved storage-ring conditions like top-up mode and fast orbit feedback (FOBF); (iii) re-design of the entire beamline set-up including construction of a new high-flux monochromator; (iv) new detection schemes in resonant diffraction and reflection based on improved experimental chambers, and (v) an upgraded pump–probe scheme based on a twin laser amplifier set-up combined with an optical parametric amplifier at the experiment in order to explore the dynamics after resonant optical excitation of specific quantum states.

2. Principles of femtoslicing in storage rings and special features of the BESSY II set-up

The slicing method to generate X-ray pulses of sub-picosecond duration was pioneered at the Advanced Light Source (ALS) in Berkeley, USA (Zholents & Zolotorev, 1996; Schoenlein *et al.*, 1996, 2000) using soft X-rays from a dipole. The method is based on the laser-energy modulation of a part (a temporal 'slice') of the electron bunch in a planar wiggler (see Fig. 1) and a subsequent separation of X-rays that are emitted in a downstream 'radiator' from electrons being excited by the laser field close to a maximum energy modulation of the electrons $\Delta E_{\max}$. In first order, this value depends only on the laser pulse energy A_L according to

$$(\Delta E)^2_{\max} \cong 4\pi\alpha A_L \hbar\omega_L (N_w/N_L), \quad (1)$$

as derived from Zholents & Zolotorev (1996) (see also Zholents & Holldack, 2006). Here A_L is the laser pulse energy, α is the fine-structure constant, ω_L is the laser frequency (resonant to the on-axis radiation of the wiggler, 800 nm wavelength), N_w is the period number of the wiggler and N_L is the number of optical cycles in the laser pulse at ω_L. If $N_w = N_L$ (ideal case), $\hbar\omega_L = 1.55$ eV one obtains $(\Delta E)_{\max} = 20$ MeV at $A_L = 1$ mJ. For medium-energy storage rings like BESSY II ($E_0 = 1.72$ GeV) this corresponds to a relative energy change of $(\Delta E)_{\max}/E_0 = 1.2\%$, which is about one order of magnitude larger than the natural energy spread of 0.08% at BESSY II. All experience shows that $(\Delta E)_{\max}/E_0$ for good slicing experiments has to be of the order of ∼1%, a figure which can be achieved by commercially available Ti:Sa lasers of few kHz repetition rate and ∼1–2 mJ pulse energy. It is easy to derive that high-energy storage rings would rather need 10 mJ or more to obtain $|(\Delta E)_{\max}/E_0| \simeq 1\%$. Since only a part of the bunch is used at few kHz repetition rates, the time-slicing technique inherently reduces the average flux from the source by the ratio R,

$$R = \eta \frac{I_b}{I_0} \frac{\nu_L}{\nu_{rev}} \frac{\sigma_L}{\sigma_b}, \quad (2)$$

where I_b/I_0 is the current fraction of the so-called 'camshaft' or 'hybrid' bunch (I_b = 5–10 mA) of the total ring current I_0 = 300 mA, ν_L/ν_{rev} is the ratio of the laser frequency and the

revolution frequency (6 kHz and 1.25 MHz at BESSY II, respectively) and η is the number of modulated electrons within the observation window ($\eta \simeq 10$–20%). The ratio of the r.m.s. durations of the laser $\sigma_L = 19$ fs and the electron bunch $\sigma_b = 20$ ps (5 mA at BESSY II) controls the fraction of the bunch charge that contributes and gives a proportional X-ray flux reduction of $\sim$1000 leading to a total $R \simeq 10^{-8}$. With the values from (1) and (2) we can already state here the following: first, medium-energy third-generation storage rings like BESSY II with short natural bunch lengths are well suited to operate a slicing facility with turn-key laser systems; second, an upgrade of BESSY II towards shorter r.m.s. bunch lengths preserving the bunch charge can potentially considerably boost the performance of a femtoslicing facility further.

In order to separate light from the energy-modulated electrons, either a vertical (at the ALS; Schoenlein *et al.*, 2000) or a horizontal separation scheme [BESSY II, Swiss light Source (SLS)] is possible [compare Khan *et al.* (2006) and Ingold *et al.* (2007)] which allows for much higher signal-to-background and is orthogonal to the vertical dispersion plane. Regardless of the separation scheme, the portion (η = 10–20%) of modulated electrons that radiate into the observation window (red hatched area in the inset of Fig. 1) depends also on the settings of the radiator, since the angular distribution emitted from it is wavelength- and polarization-dependent. We use light from electrons with $\Delta E < 0$, in order to avoid background from the downstream ring dipole that emits its light swath to the other side. However, the energy-dependent width of the radiation cone sets us a lower limit of $\sim$250 eV, where the separation of short-pulse photons from the background becomes challenging especially in the case of elliptical radiation at large undulator deflection parameters K.

If both the radiator and the modulator are in the same straight section separated by a dispersive element, the slicing scheme can be, from the accelerator point of view, considered like a transfer line and is thus independent of the storage-ring optic, which was indeed recently changed at BESSY II for the top-up mode with no impact on the slicing performance. Alternative approaches that use the dispersion of ring dipoles have been proposed but not yet been demonstrated (Nadji *et al.*, 2004; Yu *et al.*, 2011; Lau, 2012). Realising these schemes would allow for using two or even more radiators along the ring.

Aiming at generating femtosecond pulses of variable polarization and using them within an optical pump–X-ray probe set-up, we use a U139 as 'modulator', a planar wiggler of 10 periods (see Khan *et al.*, 2006), and a UE56, an elliptical undulator of 30 periods, as 'radiator', as indicated in the floor plan of the facility drawn in Fig. 2 to illustrate overall dimensions and pathways of electrons, X-rays and laser pulses throughout the facility ($\sim$50 m). The scheme depicts the natural synchronization between the lasers and the X-ray beam since the main 'clock' for everything is the Ti:Sa oscillator which is the origin of both the amplified pump pulse as well as the X-ray pulses. It is synchronized to the master clock of the accelerator (with 300 fs accuracy) to hit always the maximum of the electron bunch [$\sim$50 ps (FWHM)] with sufficient temporal precision.

We mentioned elsewhere (Holldack *et al.*, 2006) that the path length differences of the energy-modulated electrons create a sub-picosecond dip and side lobes in the longitudinal bunch profile, which gives rise to intense coherent THz radiation. Using a dedicated THz beamline at a bend magnet 11 m downstream of the modulator (marked green in Fig. 2), the laser/electron-beam overlap can be found and optimized and maintained by feedback loops controlling two laser mirrors and the synchronization between laser and storage ring.

In its current state, the pump–probe scheme allows for an easy switching (within minutes) between X-ray pulses of $\sim$50 ps (σ_b = 20 ps) and $\sim$100 fs pulse length (FWHM) by choosing photons either from regular electron bunches or

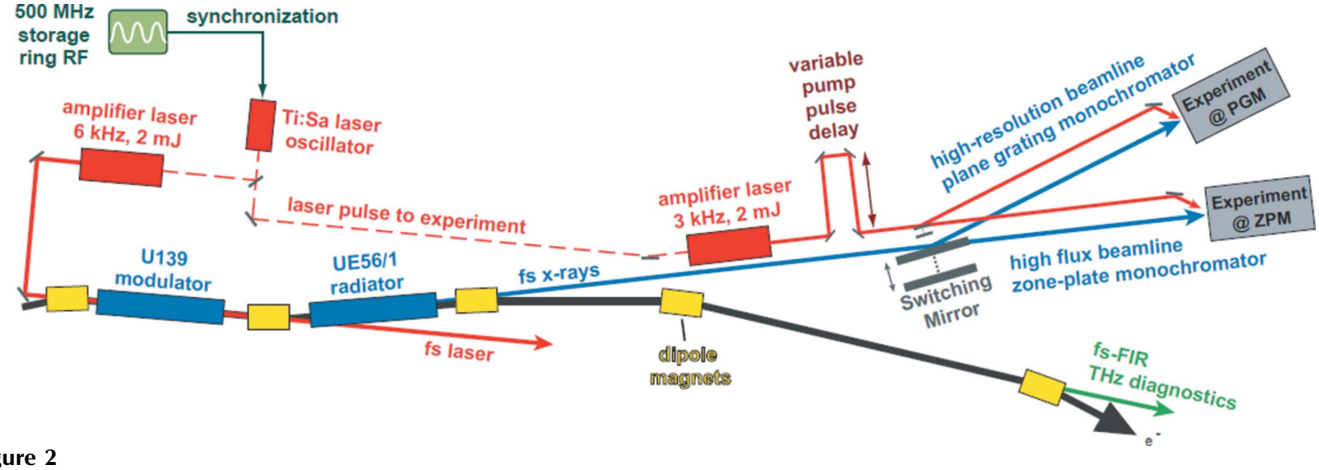

Figure 2
Schematic layout of the full optical pump–soft-X-ray probe set-up at the FemtoSpeX facility after the laser (red boxes) and repetition rate upgrade. The horizontal dimension of the entire set-up is $\sim$50 m. Synchronized to the 500 MHz master-oscillator driving the RF cavities of the ring, a Ti:Sa oscillator seeds the two regenerative amplifiers that are located in different laser hutches. Both the X-ray beam (blue) and the laser beam (red) travel a similar pathway (in-vacuum) to the experiment, while part of it is bridged by the transversely actively stabilized oscillator beam (dashed red line). As a monochromator, either the high-resolution plane grating monochromator (PGM) or the high-flux zone plate monochromator (ZPM) can be selected by setting a switching mirror to the corresponding position.

from the energy-modulated electrons employing a variable kick in the electron beam's path according to Fig. 1. Hence, the beamline can always stay aligned on-axis with the UE56, while the electron beam is statically steered such that the energy-modulated electrons are kept on-axis within the undulator causing the photons to point on-axis into the beamline. Operating the two amplifiers at 6 kHz (probe pulse) and 3 kHz (pump pulses) as indicated in Fig. 2 enables us to detect both the unexcited and excited state of the sample on a short time scale analyzing subsequent shots.

We can state here that the strength of the BESSY II femtoslicing source is mainly a combination of the facts that it is based on an APPLE II undulator, the 100 fs probe pulse length at natural synchronization and the excellent signal-to-background in the soft X-ray range thanks to the variable horizontal separation scheme.

2.1. Twin laser amplifier set-up at 6 kHz repetition rate

To address resonant pumping at high repetition rates, the new laser system consists of two coupled Ti:Sa amplifiers (Legend Elite Duo; COHERENT) driven by the same oscillator (Micra; COHERENT). The amplifiers typically run at 6 and 3 kHz for the slicing and the pump excitation, respectively, and at pulse energies of 1.8 mJ. This energy is sufficient to feed an optical parametric amplifier (Opera Solo; COHERENT) delivering variable pump wavelengths from UV to the far-IR, even though the lower pulse energy, 220 µJ at 240 nm, 6 µJ at 18 µm, might be too low for certain multi-color experiments.

The new coupled separated twin amplifier system is a challenging approach: the need to seed the second amplifier from a laser oscillator which is about 40 m apart makes it more complex and fragile to spatial drifts. This has been overcome by an active stabilization of the seed laser path which is fully in-vacuum. Although both amplifiers are naturally synchronized by the joint seed laser, additional sources of timing jitter or drifts are: (i) the index of refraction of air as a function of humidity, barometric pressure, and, even more important, (ii) relative path length drifts within the two amplifiers. The first is minimized by in-vacuum transfer lines, temperature-stabilized laser hutches and active transverse feedback stabilizations of the beam path between the two amplifiers. More serious are changes of path lengths (delay) and also pulse length (chirp) due to variation of the temperature of the laser base plate (and its optical elements) and thus path length changes in the regenerative amplifier and the stretcher/compressor section of the laser. This is mainly the case after starting the lasers. Therefore, it is a prerequisite for a stable time resolution that both laser amplifiers have a proper warm-up time to reach thermal equilibrium. It turned out that after warm-up times of $\sim$2 h for both lasers such effects do not reduce the overall time resolution anymore. However, a start from scratch after a restart of the lasers always requires a check of time-zero at the experiment on the femtosecond scale.

After two years of operation of the twin amplifier scheme we can state that the time resolution of pump–probe experiments with the new laser system is still 120–150 fs over a period of a day. It is given by the probe pulse length of $\sim$100 fs, the pump laser's pulse duration of <40–80 fs (including the discussed path length effects) and elongation by the X-ray optics ($\sim$30 fs). Experiments (Eschenlohr *et al.*, 2013; Radu *et al.*, 2014; see also §5.1) confirmed an upper limit of the time resolution of 140 fs by benchmark experiments based on time-resolved XMCD with 10 fs precision. The X-ray pulse duration, *i.e.* the resolution limit, of 100 fs is very stable (a few femtoseconds) and only determined by the slicing laser's pulse length (40 fs) and additional path length differences of the electrons along their (only $\sim$2 m) long track between modulator and radiator (Khan *et al.*, 2006).

2.2. Brilliance and flux at 6 kHz repetition rate

Another important property of the new pump–probe set-up at the UE56 is that the regular bunches [$\sim$50 ps (FWHM) at BESSY II] as well as compressed bunches in the low-α mode [<10 ps (FWHM); Jankowiak & Wüstefeld, 2013] can be employed at 6 kHz with higher flux but different time resolution. As depicted in Fig. 3, the average brilliance of the slicing mode is dramatically reduced by $\sim R$ [see equation (2)] and the number of femtosecond-photons from the undulator is now $\simeq 10^7$ photons s^{-1} (0.1% bandwidth)$^{-1}$ from the radiator which translates to $\sim 10^5$ to 10^6 photons s^{-1} (0.1% bandwidth)$^{-1}$ detected at the sample behind the ZPM monochromator ($\sim$100–1000 photons pulse^{-1} at 6 kHz). Preferentially, the third and fifth harmonics from the UE56 are used. It has been demonstrated in many publications (*e.g.* Stamm *et al.*, 2007, 2010; Radu *et al.*, 2011; Boeglin *et al.*, 2010; Holldack *et al.*, 2010; Wietstruk *et al.*, 2011; Pontius *et al.*, 2011;

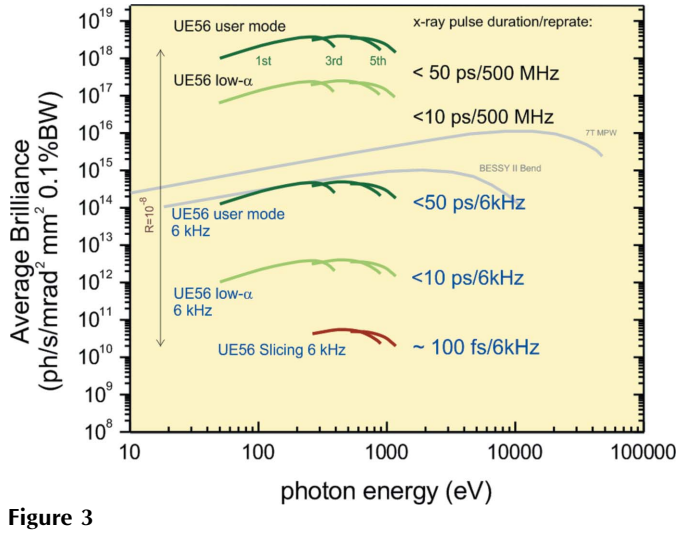

Figure 3
Available average spectral brilliance from the UE56 and maximum repetition rate of selectable different time-resolved operation modes at different X-ray pulse length. The 500 MHz would correspond to the case that all 400 buckets in the ring would be filled with electrons. In the slicing case (as reduced by $R = 10^{-8}$), the lower energies are not accessible owing to limits of separating light from sliced electrons at large natural opening angle of the undulator's central radiation cone (photon energy < 250 eV). Peak brilliance in femtoslicing is $\sim 10^{22}$ photons s^{-1} (0.1% bandwidth)$^{-1}$ mrad^{-2} mm^{-2}.

Eschenlohr *et al.*, 2013; Bergerard *et al.*, 2014) that this is a convenient flux for ultrafast optical pump–X-ray probe studies.

3. State of the art of femtoslicing at BESSY II

Ultrafast magnetic experiments require circularly polarized soft X-ray pulses particularly at the *L*-edges of the transition metals and *M*-edges of the lanthanides (covered by the UE56; see Fig. 3). However, employing polarized light from elliptical undulators in combination with the slicing technique has additional issues arising from the special angular emission properties of elliptical undulators. A crucial feature at BESSY II is the possibility to easily switch between picosecond and femtosecond pulses by a variable kick in the electron beam on user's request, an outstanding property to find time-zero in pump–probe experiments. With the upgrade of the laser repetition rate we solved a fundamental problem that limits the signal-to-background ratio due to the so-called 'halo' effect (Streun, 2003). This halo is a result of the persistence of the electron bunch's excitation from a previous slicing process that lasts $\sim$1 ms (order of the storage ring's transverse damping time) and results in an increased emittance (of the slice) adding enhanced picosecond background to the femtosecond X-ray pulses. This background becomes significant for slicing repetition rates above 1 kHz. The concept to solve this problem we named 'sequenced slicing' has been successfully used as regular user operation mode after the upgrade to 6 kHz.

3.1. Variably polarized X-rays of $\sim$100 fs pulse duration

As mentioned above, FemtoSpeX at BESSY generates the X-ray probe pulses *via* an elliptical undulator of the APPLE II type (Sasaki *et al.*, 1992; Bahrdt, 2012). Higher-harmonic generation (HHG) and FEL sources use quarter-wave plates in order to employ circularly polarized X-rays in that energy range (Graves *et al.*, 2013); APPLE II undulators and crossed undulators for the vacuum-ultraviolet (VUV) range are proposed or exist at the FERMI-FEL (FERMI, 2013). The full tunability of an elliptical undulator with respect to energy and polarization has been the main reason that experts in ultrafast magnetism are attracted by our facility, since optical pump–polarized X-ray probe experiments at the *L*-edges of transition metals and *M*-edges of lanthanides with $\sim$100 fs time resolution are still difficult at other sources. While pump–probe studies of magnetic dynamics with table-top sources have been recently made with linearly polarized VUV pulses from HHG sources (Turgut *et al.*, 2013), magnetization dynamics is probed there only incompletely, not in absolute terms of the magnetic moments and not resolved with respect to spin and orbital angular momentum as in complete X-ray magnetic circular dichroism (XMCD) measurements (Stamm *et al.*, 2007).

The XMCD technique requires the use of energetically tunable elliptically polarized X-rays as emitted from elliptical undulators. In the following we will discuss how the choice of polarization affects the separation of the short-pulse component from the main cone of the synchrotron beam. The key ingredient of femtoslicing on the basis of horizontal separation is the horizontal width $\sigma'_{\rm h}$ of the main cone of synchrotron radiation from the UE56 radiator. Next to the finite source effects, *i.e.* the natural horizontal emittance of the storage ring, $\sigma'_{\rm h}$ depends largely on the undulator parameters, namely the undulator *K*-value and the harmonic number. Using the formula for the angular distribution from Kim (1986) but taking into account only its horizontal projection $\sigma'_{\rm h}$, and applying BESSY II and UE56 parameters for undulator period $\lambda_{\rm p}$ = 56 mm, 30 periods, harmonic number n and $\gamma = E_0/mc^2$, we arrive at

$$\sigma'_{\rm h} = 3\left\{\frac{1 + \left(5.23\,[\text{cm}] \times B_{\rm v}\,[\text{T}]\right)^2/2}{60n}\right\}^{1/2} \text{mrad}. \qquad (3)$$

It is seen that $\sigma'_{\rm h}$ increases close to proportional to the applied vertical magnetic field $B_{\rm v}$ and obviously will be minimized when $B_{\rm v}$ = 0, *i.e.* for vertically polarized light settings. This requires a shift of the UE56 magnet structures of $\pm$28 mm. As the shift is reduced (elliptical polarization), $\sigma'_{\rm h}$ increases and reaches its maximum at shift = 0 mm, *i.e.* for horizontal linear polarization. This can be shown experimentally by measuring the photon flux at 700 eV at the end of the monochromator. Its acceptance is set fixed to 0.1 mrad $\times$ 0.1 mrad when tuning the electron bump. The result is given in Fig. 4(*a*) revealing a much narrower horizontal distribution for the linear vertical case as predicted by the calculated results obtained using the *SRW* code (*Synchrotron Radiation Workshop*; Chubar & Elleaume, 1998) for respective parameters given in Fig. 4(*b*).

The good agreement with experimental data is also consistent with simulations with the *WAVE* code (Scheer, 2012) as used earlier in Fig. 1. In the real circular operation mode (shift 18 mm; see Fig. 5*a*) of the UE56, the beam becomes donut-shaped and a horizontal separation of the femtosecond signal can only be achieved using very large deflection angles >1 mrad. However, using larger shifts (25 mm in our case, 'vert. ell.' in Fig. 5*a*), elliptical polarization of high degree of circular polarization ($P_3 > 0.7$) is emitted at narrow beam. In this case the polarization ellipse (and the angular intensity distribution) stands vertically rather than lying horizontally like in horizontal planar operation. This way, it is possible to achieve both sufficient elliptical polarization of the X-rays *and* a reasonable separation of them from the main radiation cone at small 'bump' settings.

A further issue complicates the application of elliptically polarized femtosecond X-ray beams within the scheme of angular separation: the relativistic Lorentz contraction leads to a strong forward emission of the synchrotron radiation. However, emission observed from more than about $2/\gamma \simeq$ 0.6 mrad at BESSY II appears in the laboratory frame opposite in helicity than the on-axis emission. This results in a background component that is inversely polarized to the main signal. In cases of a poor signal-to-background ratio this fact might severely obscure the results by dilution of the polarization degree. One can get rid of this by thoroughly

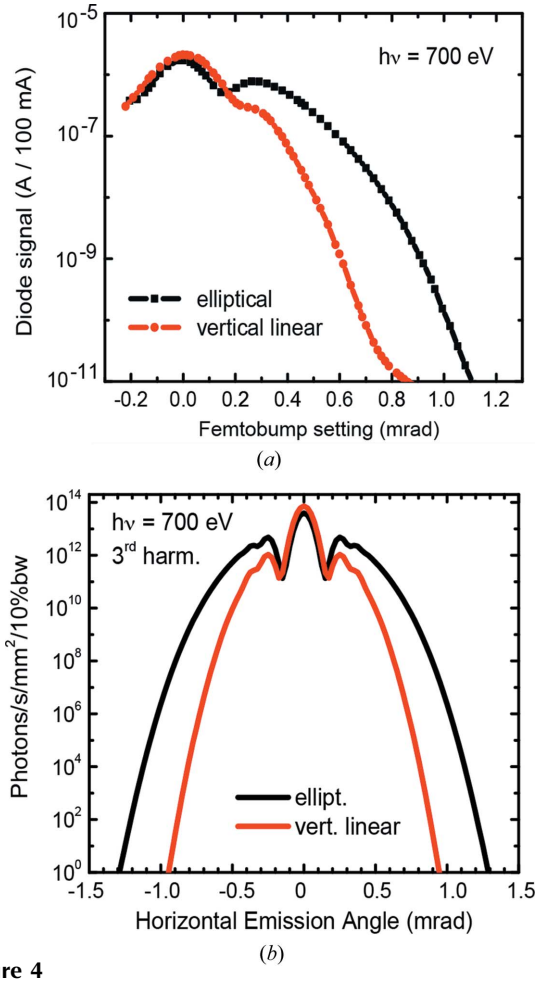

Figure 4
(*a*) Measured horizontal angular distribution of light from the UE56 for elliptical (black) and vertical linear (red) polarization at a photon energy of 700 eV at 0.1% bandwidth. (*b*) Corresponding calculated (with *SRW* code; Chubar & Elleaume, 1998) horizontal width of the full UE56 emission cone at 700 eV for the case of elliptical (black) and vertical linear (red) polarization.

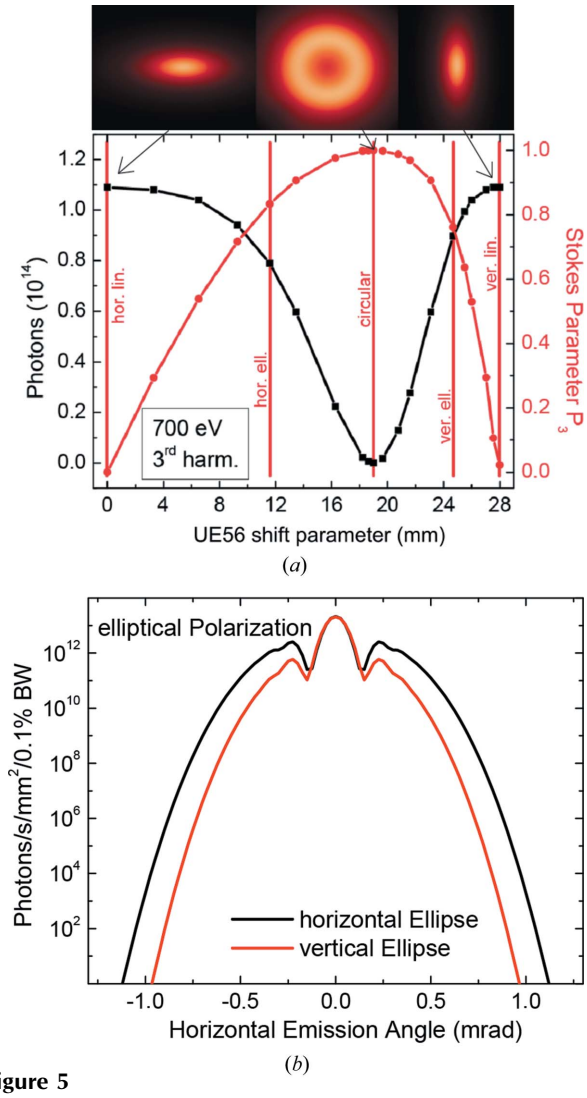

Figure 5
(*a*) Calculated on-axis X-ray intensity and Stokes parameter $P_3 = S_3/S_0$ (ellipticity) as a function of the radiator's shift parameter for $h\nu = 700$ eV in the third harmonic and footprints of the monochromatic beam 10 m from the source at different polarization states (images calculated with *WAVE*; Scheer, 2012). (*b*) Calculated emission cone (with *SRW*; Chubar & Elleaume, 1998) at 10 m from the source for horizontal (red) and vertical ellipses (black). The beam is horizontally much narrower for the vertical elliptical case (at a shift of ~24.5 mm).

controlling the acceptance of the beamline by vertically collimating slits combined with additional slits in the focal plane. For an exact determination of the XMCD signal it is further important to apply a reliable background subtraction.

3.2. The 'femtobump' concept: easy switching between picosecond and femtosecond time resolution

The horizontal separation is controlled by the so-called 'femtobump' which is a horizontal closed orbit bump of the electron beam along the radiator (see Fig. 6). It is used to kick the energy-modulated electrons (lower energetic electrons, $\Delta E/E_0 \simeq -1\%$) onto the radiator's axis and regular electrons away from it. Implementing this bump setting, performed within minutes on user's request, one can easily switch between ~50 ps time resolution and ~100 fs time resolution without changing anything else. As far as we know, this is a unique feature at BESSY II since there is no angular separation implemented at the ALS (Schoenlein *et al.*, 2000) and no bump-based control of slicing at the SLS design (Beaud *et al.*, 2007).

The variable horizontal kick in the electron beam is crucial to preserve the polarization properties of the 100 fs pulses as they have to be emitted from on-axis electrons in the UE56. However, not to disturb others, a decoupling of the slicing activities from experimental conditions around the rest of the storage ring is enabled by a set of compensating feed-forward configurations. From an accelerator point of view the femtosecond-slicing straight section consists of two undulators and three dipoles, *i.e.* a 0.56 m-long central dipole and two 0.28 m-long dipoles upstream and downstream from the undulators, providing a static triangular bump separating the axes of the undulators. An additional variable closed triangular bump (the 'femtobump'; see Fig. 6) allows for horizontal pointing

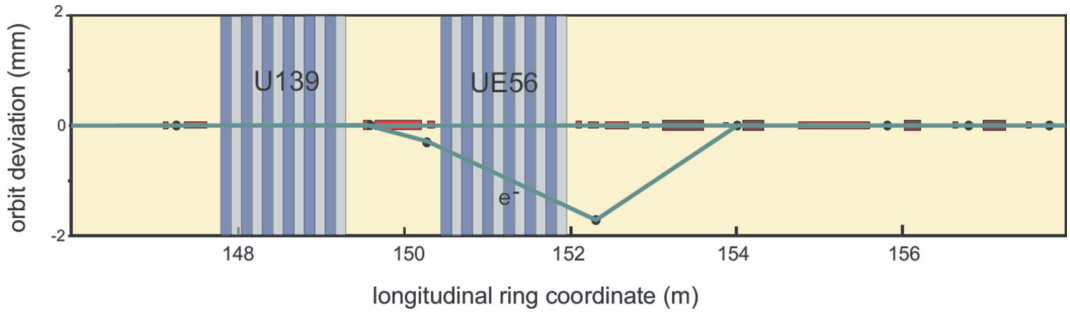

Figure 6
Schematic (undulators not drawn to scale) of the horizontal electron orbit manipulation along the slicing straight section in the storage ring showing the displacement of the electron beam along the two undulators (blue bars) at a 'femtobump' setting of −0.8 mrad relative to the regular orbit as controlled by the FOFB. The horizontal displacement (green) of the electron beam as measured by the beam position monitor readings (black dots) indicates the triangular bump along the radiator (UE56) with up to 2 mm horizontal displacements. Note that photons from displaced electons are not used, only femtosecond photons travelling on-axis. Positions of dipoles (including the short ring correctors) and sextupoles and quadrupoles are displayed in red.

control within the radiator, covering a range from 0 to ∼1 mrad, well suited for blocking the core beam and optimal usage of the 'sliced' photons. Orbit kicks and focusing effects of the insertion devices involved are compensated like in any other straight at BESSY with internal dipole correctors in the insertion devices as well as by additional gap- and shift-dependent currents in the ring quadrupoles. The variable photon-separating triangular bump is created by additional currents in the middle and closing dipole of the chicane; for bump closure the next horizontal storage-ring dipole corrector is used.

Focusing effects are compensated by additional currents in adjacent quadrupoles and the additional path length change of the electron beam is corrected by adjustment of the RF frequency. Imperfections of this feed-forward scheme are flattened out by the fast orbit feedback (FOFB). With these compensations, pointing in the radiator can be changed by 0.02 mrad s^{-1} on user's demand without measurable effects outside the femtosecond-slicing facility and with convincing reproducibility.

3.3. Photon energy differences

Although the sliced electron bunch travels along the undulators and beamline axis, one has to be aware of the fact that the average photon energy of photons from the slice is different. According to the analytic undulator formula, one obtains for the energy in the nth harmonic,

$$E_{\rm ph} = n\,\frac{2\gamma^2 hc}{\lambda_{\rm p}[(K^2/2)+1]} \qquad (4)$$

with γ = 3366 at 1.72 GeV, the deflection parameter K for a shift of 25 mm is tabulated as derived from the real field maps of the UE56/1; hc is 1.237 × 10^6 eV m, the electron rest mass m = 0.511 MeV/c^2, the period length $\lambda_{\rm p}$ = 5.6 cm. For, say, the Gd-M_5 edge at 1185 eV on the third harmonics in circular mode, one obtains K = 0.734 at an on-axis gap of 34.8 mm. Since we use the 'loss' electrons, the electron energy E is lower and the corresponding K-value (and the peak field) has to be lower to compensate for that. A recently measured optimum gap setting of 35.5 mm for 1185 eV indicates, according to equation (2), an average energy loss of $\langle \Delta E/E \rangle$ = 0.65% of electrons in our observation window and at laser parameters of 9 W at 6 kHz (1.6 mJ).

The value of the 'femtobump' is correlated with the energy modulation since the latter is translated by dispersion (B = 1.13 T of the central dipole) into a horizontal deflection. If the value of the variable bump is too high, only red-shifted photons travel on-axis along the beamline and the harmonic becomes wider in energy *and* appears at larger gap setting. Using a smaller bump one can compensate for this but at the expense of an increased background.

A commissioning example of how the femtosecond X-ray intensity depends on the initial energy modulation is depicted in Fig. 7. The intensity and width of the harmonic scales non-linearly with the laser power, a consequence of the separation scheme. The different photon energy according to equation (4) has to be taken into account by changing the gap and shift settings of the radiator by feed-forward tables according to

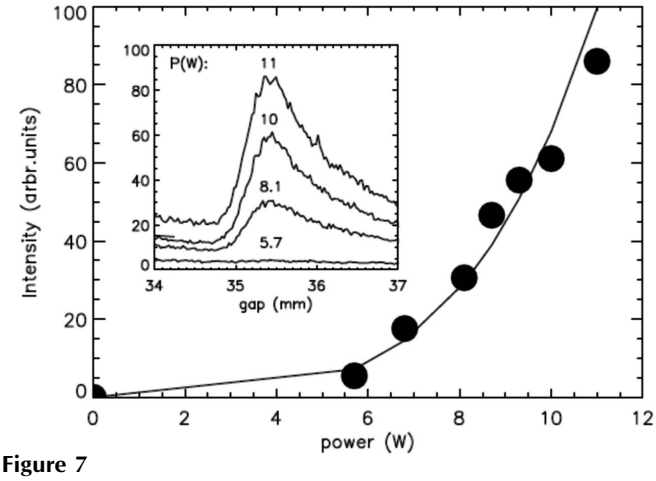

Figure 7
The third harmonic from the UE56 under slicing conditions at 1185 eV in elliptical mode (inset) and their peak intensity measured with sliced photons at 1185 eV (dots) for a shift parameter (see Sasaki *et al.*, 1992) of 25 mm and a femtobump setting of −0.75 mrad taken at different power settings P (W) of the slicing laser (single sweeps, 0.5 s per data point). Asymmetry of these peaks is due to finite acceptance (∼0.1 mrad × 0.1 mrad, red-shifted photons accepted). At P = 5.7 W (<1 mJ), the short pulse component is completely hidden behind a picosecond background, hence a power level of >6 W (1 mJ) is mandatory; routine operation requires >9 W.

equation (2). Fig. 7 also clearly reveals that pulse energies below 1 mJ (<6 W) in the slicing amplifier are not sufficient to support femtoslicing with elliptical polarized X-rays.

3.4. Solving the problem of femtoslicing at higher laser repetition rates

It is well known and already predicted by Zholents & Zolotorev (1996) that energy-modulated electrons emit photons also after many revolutions ('halo background'; see also Streun, 2003) until their transverse elongation disappears within a damping time of a few milliseconds. If the excited bunch is hit by the laser again before the oscillation is down, which happens at repetition rates >1 kHz, a stationary oscillating X-ray 'halo' background of picosecond pulse length shines into the beamline together with the femtosecond pulses (see Fig. 8*b*). We suppress halo background by using a special storage-ring filling pattern combined with a special sequential pulse-picking technique within the laser system (Fig. 8*a*). The accelerator mode takes advantage of the reduced synchronous phase drift along the bucket number of temporarily adjacent bunches. The synchronization of the femtosecond-laser amplifier (6 kHz) with the storage ring is modulated by a novel fast electronics (see Quast *et al.*, 2008) such that the slicing process periodically alters between three extra bunches on the multibunch train with a mutual temporal delay of 12 ns or multiples of 12 ns.

The bunch spacing has to be mod(12 ns), since 12 ns corresponds to the Ti:Sa oscillator's round trip time as illustrated in Fig. 8. In order to achieve an enhanced slicing intensity, the according bunches are filled with more charge (5 mA bunch current) than bunches from the regular multibunch train (∼0.7 mA per bunch). Applying this sequenced slicing mode, the transversally excited electrons in the sliced bunch have sufficient time to ring down until the next slicing process occurs [see inset in Fig. 8(*b*)]. Other options [special fill patterns with several dark gaps as proposed by us (Khan, 2005)] are not necessary. Recent highlights in ultrafast magnetism achieved by our user community (see further below) were only possible by a routine operation of sequenced slicing in BESSY II's regular user mode combined with a special fill pattern, the variable bump and the *top-up* mode which nicely keeps the X-ray signal from the camshaft bunches constant within margins of a few percent.

Introducing the top-up mode at BESSY II involved a considerable modification of the electron optic. But, the slicing schemes at BESSY II and the SLS, where modulator and radiator are located in a single high-β straight section, are very tolerant against changes of the storage ring optic. Right after its implementation in 2011, we demonstrated that the slicing performance in the new top-up optic is only weakly affected (see Fig. 9) and seems even slightly improved. Fortunately, as expected, a huge enhancement of the overall stability by the top-up mode with FOFB given by the constant bunch current has been finally achieved and former feedback controls that compensated for effects related to the decay of the camshaft bunches (∼3 h lifetime) are no longer necessary.

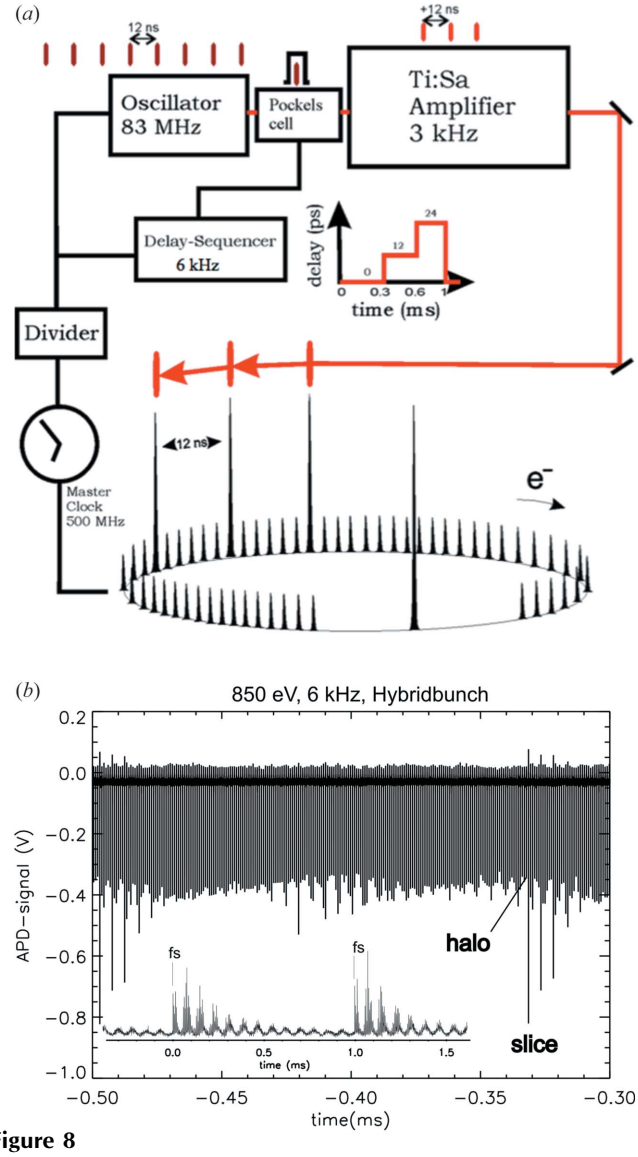

Figure 8
Schematic of 'sequenced slicing' (*a*) and the APD signal (*b*) without sequencing but at 6 kHz at the Ni-*L* edge measured at the third harmonic in elliptical mode (shift setting was 25 mm). A stationary oscillating 'halo' in the signal (negative record) remains if there is no sequence mode. The inset displays the transverse damping of the signal (positive record) in the 1 kHz case demonstrating that at 0.5 ms (*i.e.* 2 kHz) the signal is already sufficiently reduced such that the next shot may occur suggesting that hopping between three hybrid bunches at 6 kHz will lead to a background close to the 1 kHz case (see text).

4. Beamline designs for picosecond and femtosecond pump–probe applications

As depicted by the floor plan in Fig. 2, our set-up consists now of a plane-grating monochromator (PGM; Weiss *et al.*, 2001) and the upgraded zone-plate monochromator (ZPM) described in detail by Brzhezinskaya *et al.* (2013). The optical layouts of both monochromators after the upgrades are shown in Figs. 10 and 11, respectively.

4.1. Plane-grating monochromator

The PGM monochromator (Fig. 10) is based on the design by H. Petersen in the late 1980s (SX700; Petersen *et al.*, 1993)

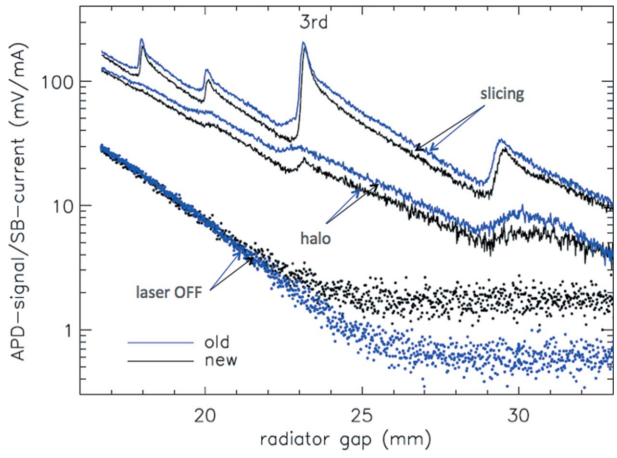

Figure 9
APD signals from the 100 fs pulses (upper) at 640 eV and the background signals (middle) for the old BESSY storage ring optic (blue) and the so-called top-up optic (black) where the horizontal β-function was reduced to $\sim$10 m in the high-β straight sections; bump = -0.75 mrad, shift = 28 mm, sequenced mode at 6 kHz. The two lowest curves represent the laser-OFF case (picosecond-leftover from core beam) and the curves in the middle arise from the 'halo' background, even lower in the top-up case.

and was improved and accommodated for the UE56 at BESSY by Sawhney *et al.* (1997). The PGM has been a workhorse for the soft X-ray spectral range from 50 eV to 2 keV at many contemporary synchrotron radiation facilities worldwide and has set spectral resolution records in that range. At the FemtoSpeX facility, the regular design is slightly modified according to Fig. 10. Here, the cylindrical mirror M3 performing the horizontal focusing is part of a split mirror unit. The pump laser beam is fed in under an angle of 1.5° approaching collinear overlap of the pump laser pulse and the X-ray spot on the sample. The monochromator is equipped with three selectable gratings (150, 400 and 1200 lines mm^{-1}). The pulse length for femtosecond applications is only preserved when using the 150 lines mm^{-1} grating ($\sim$30 fs stretching at 850 eV) at the cost of spectral resolution ($\lambda/\Delta\lambda \simeq 10^3$). The other gratings apply for picosecond-applications only, as given by the Fourier limit. The strength of the PGM beamline for pump–probe applications is mainly its high resolution when using the 1200 lines mm^{-1} grating for picosecond dynamics studies, where pulse elongation on the 100 fs level is not an issue. The latter is widely used and really indispensable in X-ray diffraction and XAS applications when spectral resolution is required to identify transient spectral features which can then be studied with $\sim$100 fs time resolution in the slicing mode at moderate bandwidths.

4.2. Zone-plate monochromator

In order to achieve the highest possible transmission (up to 21%), we have decided to use a single-element monochromator based on reflection zone plates (RZPs; Aristov *et al.*, 1988; Basov *et al.*, 1994; Wilhein *et al.*, 1997). However, the inherent feature of zone plates, *i.e.* the focal distance depends on wavelength, limits the useful bandwidth of a monochromator being based on them, unless slit or sample travel longitudinally with wavelength. The other option is to add additional surrounding mirrors compensating for this draw-

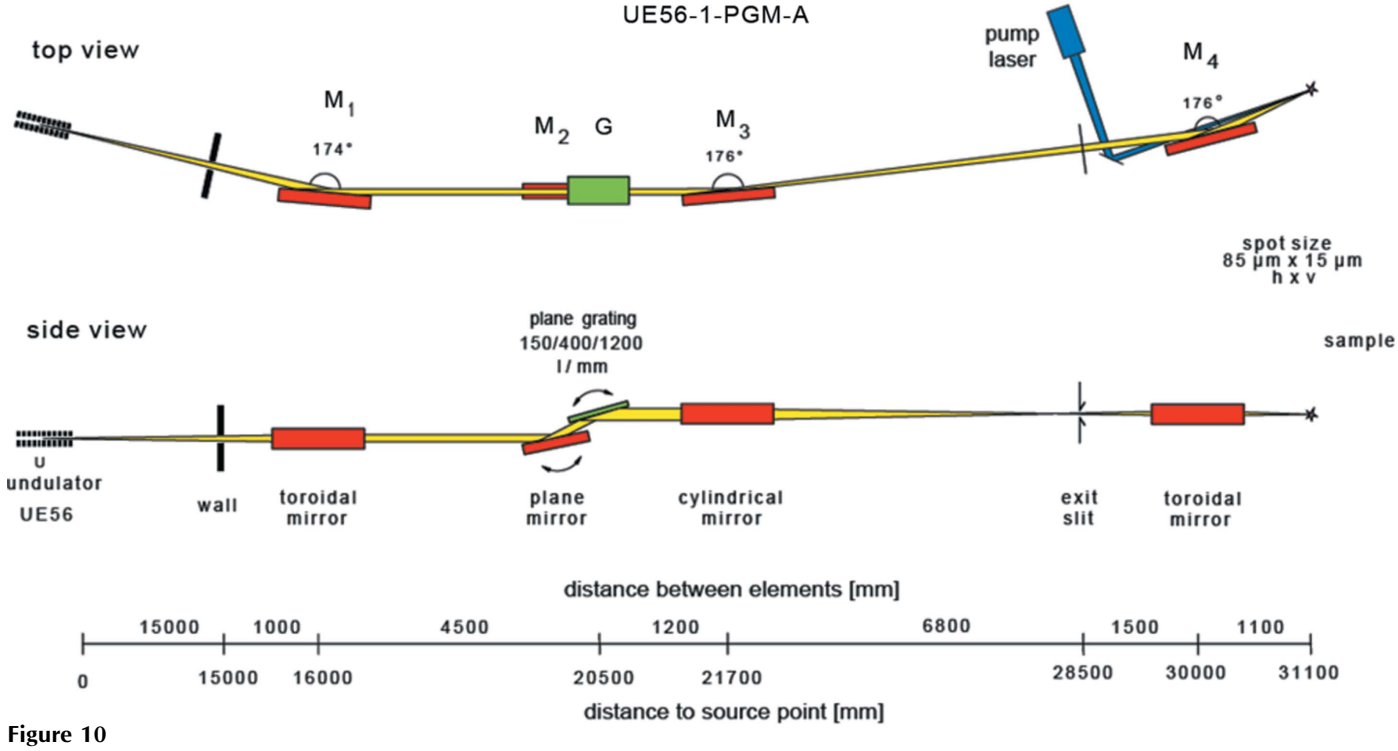

Figure 10
Optical layout of the plane-grating monochromator (PGM) at the FemtoSpeX facility after the beamline upgrade in 2010. It consists of five optical elements (mirrors M1–M4 and grating G) that limit the transmission to $T = 0.01$, an order of magnitude less than at the ZPM at the same bandwidth. Spot size is 85 µm × 15 µm (H × V) and depends vertically on the exit slit dimension.

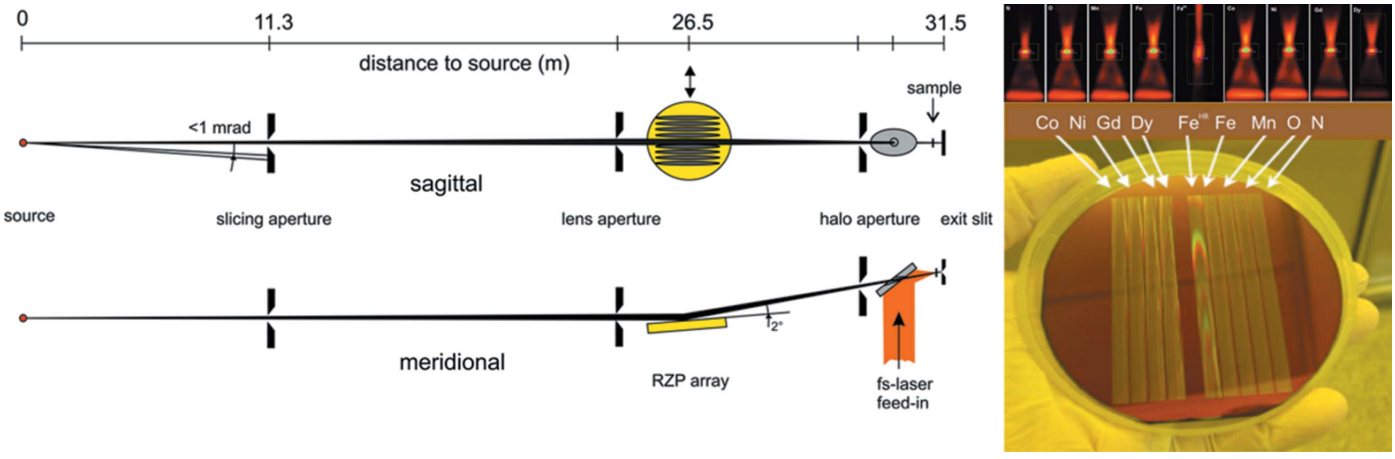

Figure 11
Optical layout (left) of the high-transmission ($T \simeq 0.2$) ZPM beamline after the upgrade in 2012. In order to select a certain lens (image) and energy range, the optical element (RZP array, yellow) is moved perpendicular to the optical axis driven by a stepping motor. A special laser feed-in (orange) is an inherent part of the approach enabling pump–probe experiments with variable pump wavelength from UV to FIR at large numerical aperture. The red images above the right-hand picture show the intensity distributions in the focus after each lens (see Brzhezinskaya *et al.*, 2013). Spot size is ∼150 µm (H) × the vertical slit dimension, *i.e.* 20 or 40 µm.

back at the expense of flux. Here, we followed the route to keep the flux advantage and to alleviate the bandwidth limit problem by using an *array* of RZPs. Under certain conditions a large energy range can be covered this way as was recently described by Brzhezinskaya *et al.* (2013). The current design as depicted in Fig. 11 (right) consists of nine lenses that enable a working range from 410 to 1333 eV at moderate spectral resolutions of $\lambda/\Delta\lambda = 500$ or, in one case, $\lambda/\Delta\lambda = 2000$, at 713 eV. A specified maximum pulse elongation of 30 fs defines the maximum aperture of the lens and the possible energy resolution. For the parameters of the lenses used in the energy range from 410 to 1333 eV, the average grating periods are $d \simeq 15$–25 µm, values that limit the lengths of the RZPs to 80 mm in each case. At 2° grazing incidence the acceptance fits well to the angular emission characteristics of the 100 fs photons.

The general optical layout as built in 2012 consists of a cubic ultrahigh-vacuum vessel containing the RZP array located at 26.5 m away from the source and mounted onto a rigid granite block that consists of two separated parts (Fig. 11, left). The upper part that holds the monochromator vessel can slide perpendicular to the beam along grinded rails in the lower base part at a precision of <10 µm (repeatability). Users can select the lens of interest, pre-aligned during commissioning (Fig. 12), driving this axis. The 100 fs X-ray and the 50 fs pump laser pulses are merged ∼800 mm upstream of the sample by a rectangular 40 mm × 60 mm broad band metal mirror with a 1.5 mm hole in the center to ensure a collinear propagation of both beams. The ZPM is usually used as a first choice for femtosecond experiments since it represents a suitable compromise between time, energy resolution and transmission. Higher spectral resolution at the ZPM ($\lambda/\Delta\lambda = 2000$) or at the PGM monochromator (>5000) is only available at deteriorated time resolution larger than the 100 fs pulse length. Using light from the normal or low-α mode, pulse lengthening plays no role and high resolution is feasible.

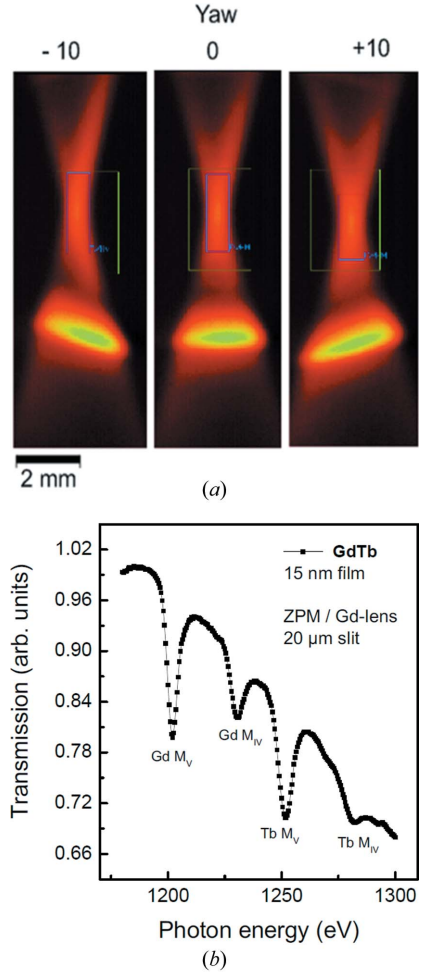

Figure 12
Examples from the commissioning of the new ZPM monochromator. (*a*) Image in the dispersion plane with the undulator's fifth harmonic set slightly below focus. If the yaw setting is detuned only by ±0.01° the orientation and symmetry of the off-focus image can be used to optimize the alignment of the lens for maximum resolution and transmission. (*b*) Transmittance spectrum from a GdTb thin film sample taken at the new ZPM after the upgrade using the Gd lens and 20 µm exit slit.

5. Methods and endstations

Owing to the special properties of photon pulses in a slicing experiment, the variety of usable synchrotron radiation methods and instruments is limited, mainly due to the low flux. Photon-hungry techniques like resonant inelastic X-ray scattering (RIXS), photoelectron spectroscopy (PES) with hemispherical analyzers, photoemission electron microscopy (PEEM) and lensless imaging are not yet supported. However, by employing special endstations the methods of time-resolved XMCD, X-ray absorption (XAS), resonant soft X-ray diffraction (RSXD) and time-resolved X-ray reflection spectroscopy (XRS) have been successfully used in many scientific applications. Time-resolved time-of-flight electron spectroscopy (TOF) is currently being developed and may most of all benefit from future upgrades.

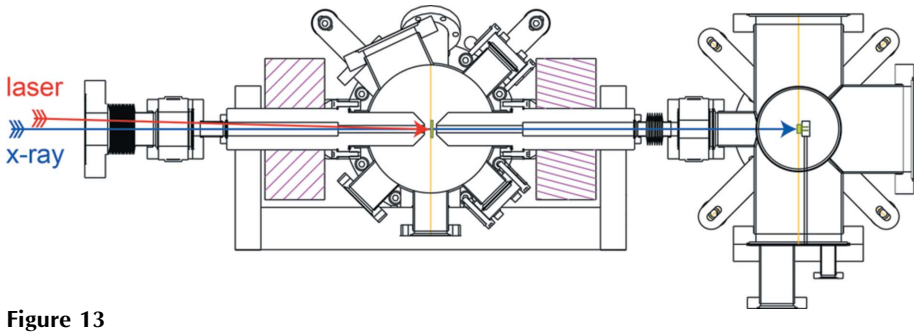

Figure 13
Layout of the experimental station for time-resolved XAS and XMCD in transmission. The left-hand chamber holds the sample and the magnetic field (coils are shaded magenta); the detector is mounted in the right-hand chamber (the blue arrow points on it). The laser pump and the X-ray probe beams both enter the sample chamber through the same flange in a collinear geometry. The laser beam is absorbed by the sample and any stray light is filtered by an Al foil mounted between the two chambers. The APD in the right-hand chamber thus detects only the X-rays transmitted through the sample. In addition, APDs feature a response time fast enough to resolve individual bunches from the storage ring. This is essential for time-gating to only measure photons coming from the laser-sliced electron bunch. Third, the transmission measurement is the most direct way for determining the absorption, which becomes important when performing the XMCD sum rule analysis.

5.1. Time-resolved XMCD and XAS in transmission

A dedicated experimental station was built to measure time-resolved XAS and XMCD (Stamm *et al.*, 2007). It makes use of the transmission geometry for several reasons. First, detecting photons is insensitive to applying magnetic fields to the sample, in contrast to a total electron yield measurement. Second, using an avalanche photodiode (APD) as detector we have the advantage of a very sensitive measurement of the low photon flux in femtosecond mode due to the inherent signal amplification in the detector.

The experimental station, sketched in Fig. 13, is capable of applying 0.5 T of magnetic field along the X-ray propagation direction. The magnetic yoke features a 8 mm hole to accommodate both the X-rays and the pump laser beam. The sample is mounted on a cryostat which allows cooling with liquid nitrogen or liquid helium, and heating above room temperature. Samples are mounted on non-magnetic plates, which are transferred into vacuum with a load-lock and transfer mechanism. The chamber is equipped with evaporators to deposit ultrathin metallic films *in situ*. The X-rays that pass through the sample are detected on the avalanche photodiode mounted in a second chamber. An Al filter in between the two chambers blocks any stray light from the pump laser from hitting the detector. The ultrafast demagnetization of a thin Ni film (Beaurepaire *et al.*, 1996) was used to test the femtosecond time resolution. Fig. 14(*a*) shows the very first pump–probe results from the slicing source in 2006 as recorded at the PGM beamline.

The dynamic response of the magnetization was measured by recording the change in absorption when flipping the magnetization in an applied field, and varying the time delay between laser pump pulse and X-ray probe pulse (Stamm *et al.*, 2007). Simultaneous to this time-resolved XMCD measurement we were surprised to also find a change in the total absorption. This additional pump-induced effect gives an independent determination of zero time delay, similar but much smaller than the changes in optical reflectivity found in laser-based pump–probe studies. The first upgrade of femtoslicing in 2010 (repetition rate 6 kHz) enabled a complete time-resolved XMCD spectroscopy including sum rule analysis in the ultrafast dynamics of the spin and orbital angular momentum per atom in the Ni film after femtosecond laser excitation (Stamm *et al.*, 2010) (see Fig. 14*b*).

The improved stability and the significant increase of femtosecond photon flux at the newly constructed ZPM

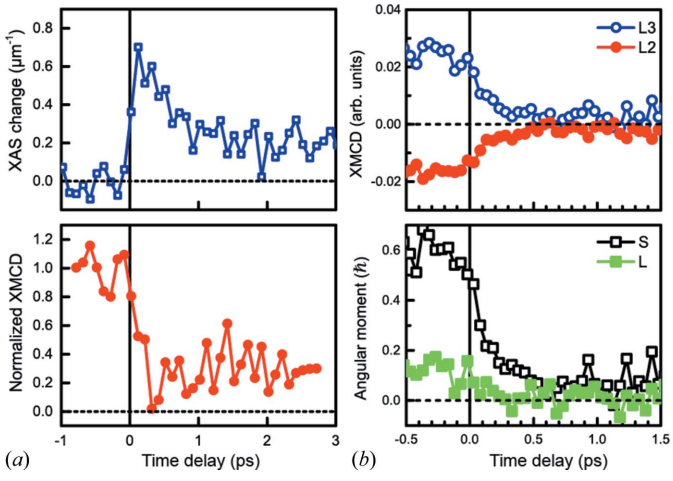

Figure 14
First femtosecond time-resolved measurement of the pump-laser-induced changes in XAS and XMCD of a 30 nm Ni film (*a*), which was excited by a femtosecond laser pulse. The X-ray photon energy was set to half of the increasing flank and to the center of the L_3 absorption edge for the XAS and XMCD measurements, respectively. The energy resolution was set to 1.5 eV for XAS and 3 eV for XMCD. A time-resolved XMCD measurement from 2010 of a 17 nm Ni film (*b*, top) and the respective XMCD sum rule analysis (*b*, bottom). The laser pump fluence was ~12 mJ cm^{-2}; the applied magnetic field was 0.24 T.

beamline dramatically increased the signal-to-noise ratio of the time-resolved XMCD measurements performed at the slicing facility, as exemplified in Fig. 15. Here we show the transient demagnetization of a 20 nm-thick Ni sample measured at the Ni-L_3-edge, a benchmark test to check the pump–probe time resolution after the upgrades. It clearly confirms that the twin amplifier scheme did not deteriorate the time resolution at all but increased the signal-to-noise considerably. Averaging over subsequently measured 12 scans corresponding to ∼1 h measurement time, one can easily achieve a signal-to-noise ratio of 0.1% in time-resolved XMCD applications.

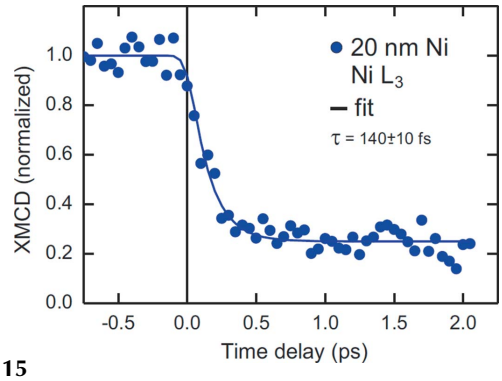

Figure 15
Time-resolved XMCD measurement of a 20 nm Ni film performed at the Ni L_3 edge taken with the twin amplifier scheme after the upgrades and with active feedback systems in operation. The blue dots are averaged data over a few hours and the black curve is a fit to the data based on two exponentials. The upper limit for the pump–probe time resolution is 140 fs as partly determined by the demagnetization time of the Ni layer (Stamm *et al.*, 2010).

5.2. Time-resolved resonant magnetic reflectivity

With a few notable exceptions (see, for example, Holldack *et al.*, 2010; Trabant *et al.*, 2013), the overwhelming majority of the time-resolved magnetic investigations at the femtoslicing facility have been performed in transmission geometry (Stamm *et al.*, 2007; Boeglin *et al.*, 2010; Radu *et al.*, 2011; Eschenlohr *et al.*, 2013). Although this approach is very powerful, it puts constraints on the geometry and thickness of the samples to be used. To enlarge the spectrum of samples that can be investigated to include bulk single-crystals or epitaxically grown samples on thick substrates, we have recently extended our experimental capabilities to reflection geometry. As model systems we investigate the transient magnetization dynamics on various magnetic metals and insulators using time-resolved XMCD in reflection geometry.

The measurement methodology is very similar to that for XMCD in transmission: we employ circularly polarized light of fixed helicity which is energy-tuned at the elemental resonance of interest and obtain the XMCD effect in reflection upon flipping the external magnetic field, which is large enough to magnetically saturate the sample. For dynamic investigations, the photo-exciting laser pulse impinges collinearly with the femtosecond X-ray on the sample in order to maintain the temporal resolution of the measurement (see the schematic drawing in Fig. 16). One such example showing both the static and dynamic XMCD effects measured at Fe edges on $Ho_3Fe_5O_{12}$ garnet is displayed in Fig. 16. The measurements were performed at a θ–2θ geometry of 10–20°. Here, demagnetization degrees up to 100% are obtained upon pumping the sample at a fluence of ∼18 mJ cm^{-2} and a wavelength of 400 nm. The observed dynamics is here limited by the time-resolution of the experiment of ∼80 ps. This θ–2θ geometry has been chosen as it provides an optimal combination of magnetic asymmetry and magnitude of the reflected signal (*i.e.* the figure of merit) together with a large pump-induced effect. As a rule of thumb, samples that possess a minimum reflectivity of about ∼10^{-5} can be considered for dynamical investigations. These are the key factors for estimating the feasibility of any time-resolved magnetic reflectivity measurement. Currently, several time-resolved magnetic reflectivity studies with ∼100 fs time resolution are on-going at the slicing facility, addressing various scientific cases on different material classes.

5.3. Time-resolved X-ray diffraction

Within the last two decades resonant soft X-ray diffraction (RSXD) has emerged as a highly efficient experimental

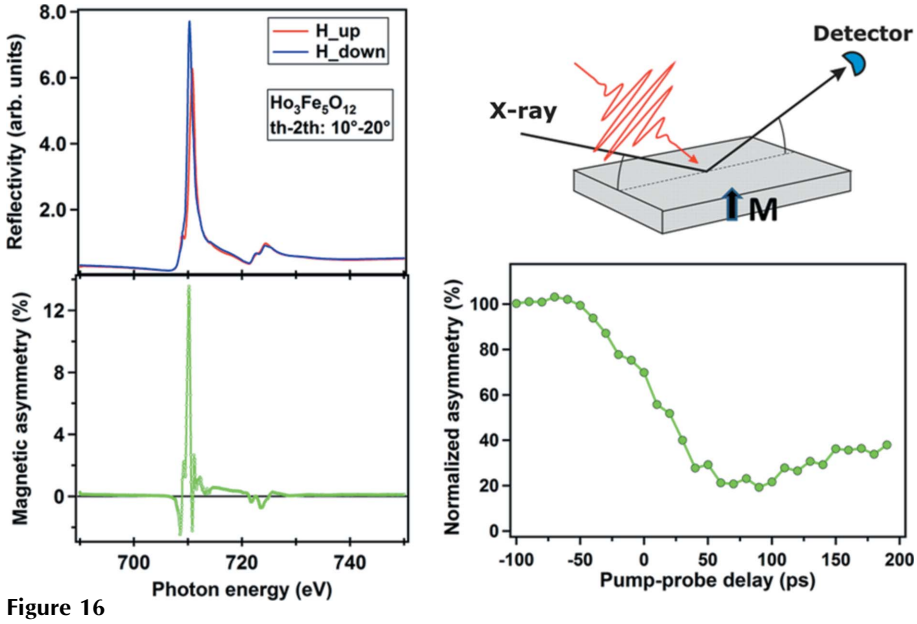

Figure 16
Left: static resonant magnetic reflectivity spectra measured for opposite magnetic fields (±10 mT) on a $Ho_3Fe_5O_{12}$ sample at 300 K and a 10–20° θ–2θ geometry. Right: schematic view of the time-resolved reflectivity geometry together with the transient demagnetization of the $Ho_3Fe_5O_{12}$ measured at the Fe L_3 edge with 50 ps time resolution upon pumping the sample at 400 nm wavelength (data taken from Radu *et al.*, 2014).

technique to probe nanoscale ordering phenomena in solid-state materials (Fink *et al.*, 2013). Beyond conventional Thomson charge scattering, RSXD is an element- and site-sensitive technique. It involves a photon absorption–emission process through the *resonant* excitation of a particular optical transition from a core level to an empty electronic valence state. For this reason RSXD combines the strengths of X-ray scattering and spectroscopy to probe spatial modulations of particular electronic valence states or spin orientation.

The inherent momentum resolution allows conclusions on spatial aspects like coherence lengths and period lengths. The ordering phenomena that can be probed involve electronic order, like charge or orbital order, as well as magnetic order. In particular, RSXD is one of the few methods that can probe antiferromagnetic order. Moreover, often information about the lattice symmetry and structure can be obtained even though long photon wavelengths give access to only a small part of reciprocal space. For these reasons time-resolved pump–probe RSXD is ideally suited to study the dynamics of photo-induced phase transitions in correlated materials when combined with ultra-short photon pulses. Within one single experimental set-up it allows mapping of all relevant physical subsystems: the electronic, the spin as well as the lattice degrees of freedom (Beaud *et al.*, 2009; Holldack *et al.*, 2010; Pontius *et al.*, 2011; Chuang *et al.*, 2013; Graves *et al.*, 2013; Johnson *et al.*, 2012; de Jong *et al.*, 2013; Lee *et al.*, 2012).

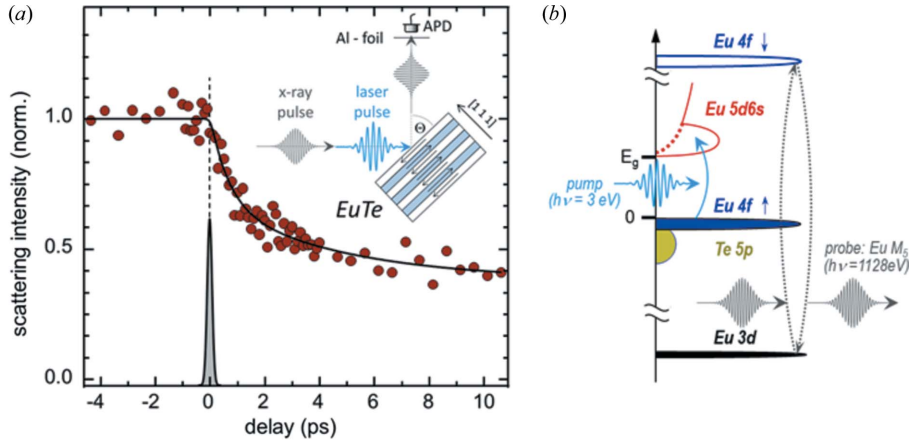

Figure 17
Time-resolved trace of the (1/2,1/2,1/2) magnetic scattering signal amplitude (*a*) of a 40 monolayer EuTe film. The RSXD signal amplitude drops within a few picoseconds before it levels at ∼40% of its original intensity. The Gaussian curve at zero delay displays the experimental temporal resolution. The inset shows a sketch of the experimental set-up. (*b*) Energy scheme of the RSXD pump–probe process.

During the past few years, RSXD has also been made available for ultrafast studies at the FemtoSpeX facility. A dedicated two-circle UHV diffractometer has been set up for diffraction geometries in the horizontal plane. By cryogenic cooling, sample temperatures down to 6 K can be reached. As for the XMCD/XAS set-up, APDs (3 mm diameter, 500 ps rise-time) are used for gated photon pulse detection. The angular acceptance of the diffractometer is set by vertical detector entrance slits of variable size and the detector distance to the sample. The APD is screened from light of the pump-laser by a ∼250 nm light-tight Al-membrane and a light-tight housing of the APD (see inset of Fig. 17). The used APD in combination with low-noise amplification allows for time-correlated single-photon pulse detection. In general, signals as low as ∼5 photons s^{-1} from the sample can be detected. This corresponds to a diffraction peak intensity of $>5 \times 10^{-5}$ times the incident photon flux.

The first compound to demonstrate feasibility of ultrafast RSXD at the FemtoSpeX facility was the antiferromagnetic semiconductor europium telluride (EuTe) (Holldack *et al.*, 2010). This study focuses on the ultrafast magnetic dynamics in an antiferromagnetic thin film of a 4*f* rare-earth chalcogenid. The samples are single-crystalline films of 40 (111) monolayers of EuTe grown by molecular beam epitaxy on BaF_2 (or PbTe) and finally capped with a BaF_2 (or PbTe, respectively). With a [111] growth direction the antiferromagnetic (AFM) order can be probed by the magnetic (1/2,1/2,1/2) Bragg peak in specular scattering geometry at the Eu-M_5 optical transition (1128 eV) resulting from the AFM superstructure (Schierle *et al.*, 2008). Since the Neel temperature of the EuTe samples is ∼12 K, the experiments were performed at ∼6 K base temperature. Fig. 17(*a*) shows the delay trace of the magnetic (1/2,1/2,1/2) scattering signal during the first 10 ps after laser excitation of a EuTe thin film between BaF_2 directly excited by 3 eV photons (see Fig. 17*b*). The data were recorded in single-photon-counting mode at a detection rate of ∼8 counts s^{-1} at 6 kHz experimental repetition rate (total recording time ∼6 h). After ∼4 ps the diffraction signal drops to about 50% of its initial value and only recovers after several nanoseconds. The used pump-fluence was ∼1 mJ cm^{-2}. Fig. 18 shows momentum-resolved scans across the magnetic (1/2,1/2,1/2) Bragg peak along the surface normal direction of a EuTe thin film between PbTe. Here, an indirect excitation of the EuTe layer has been established by using 1.5 eV photons that are

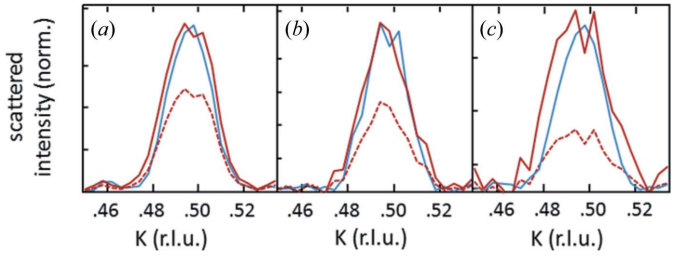

Figure 18
Momentum- and time-resolved RSXD scans along [111] across the (1/2, 1/2, 1/2) magnetic superstructure reflection. The time-resolved scans show the magnetic Bragg reflection before the arrival of the laser pulse (blue) and 500 fs (*a*), 1 ps (*b*) and 10 ps (*c*) after (dashed red). The solid red curves are the dashed ones scaled to the same amplitude as the unpumped (blue) peak.

only absorbed by the adjacent PbTe layers (0.2 eV band gap) but not by the EuTe itself (2.2 eV band gap). An increased broadening of the peak with larger delay as well as a shift of the center of mass for the 10 ps delay hint to an underlying structural sound wave dynamics that ends in a thermal expansion.

6. Future upgrades

There are four major upgrades scheduled for the next few years that will further considerably increase the average photon flux and boost the experimental capabilities at FemtoSpeX. First, the replacement of the current radiator UE56 by a newly developed in-vacuum APPLE II undulator UE30 in 2015 will yield a factor of five more femtosecond X-ray flux at about 1 keV. Second, a further laser upgrade towards higher repetition rates will directly increase the average flux. Appropriate laser systems providing few mJ pulse energies at repetition rates of up to 50 kHz and even more, *e.g.* based on optical parametric chirped pulse amplification (OPCPA) (*e.g.* Witte & Eikema, 2012) will be commercially available soon and will likely be the technology of choice to replace our existing 6 kHz twin amplifier scheme.

However, the real achievable total increase in average flux will be mainly limited by the available fill pattern which can only be a trade-off between the number of bunches *versus* possible bunch currents of additional camshaft (hybrid) bunches. This seems to set limits at repetition rates of a few tens of kHz. Third, we expect another gain by the ongoing fabrication of novel three-dimensional reflection zone plate arrays (RZPAs) with individual profile depth for each specific lens. Fourth, FemtospeX, first and foremost its photon flux, will directly benefit from longitudinally compressed bunches at preserved bunch currents in the BESSY-VSR facility (Jankowiak & Wüstefeld, 2013). This future upgrade of BESSY II will result in an increased longitudinal density of electrons in the bunch compared with now and it will give another factor of five in flux. In total, these three separate measures are expected to improve the photon flux by a factor of 125 keeping the set-up competitive among other facilities supporting ultrafast X-ray applications.

7. Summary and conclusions

We have successfully upgraded the femtoslicing facility at BESSY II. Only recently it has been gradually converted into a versatile pump–probe user facility, FemtoSpeX, operating at 6 kHz repetition rate that enables one to perform time-resolved optical pump X-ray probe experiments in the 100 fs to 50 ps (FWHM) X-ray probe pulse length regime. Further upgrades of the radiator (a UE30), a further increase of the laser repetition rate up to 50 kHz and using compressed bunches in the storage ring are planned to boost the performance of FemtoSpeX towards an average flux of $\sim 10^8$ photons s^{-1} (0.1% bandwidth)$^{-1}$. These remarkable figures will enable a new class of storage-ring-based ultrafast experiments with fully tunable soft X-ray pulses.

We are deeply indebted to the BESSY II accelerator and beamline team for comprehensive support. We are further grateful for fruitful discussions with our colleagues from TU-Dortmund, SLS and other facilities. This work was financially supported by the BMBF project 'Next generation instrumentation for ultrafast X-ray science at accelerator-driven photon sources' (project No. 05K12CB4), the FemtoSpeX project (No. 05K10PG2) and a Marie Curie FP7-Reintegration-Grant within the 7th European Community Framework Program (project No. PCIG10-GA-2011-297905).

References

Aristov, V. V., Erko, A. I. & Martynov, V. V. (1988). *Rev. Phys. Appl. (Paris)*, **23**, 1623–1630.
Bahrdt, J. (2012). *Undulators*, http://www.helmholtz-berlin.de/forschung/grossgeraete/undulatoren/.
Basov, Yu. A., Roshchupkin, D. V. & Yakshin, A. E. (1994). *Opt. Commun.* **109**, 324–327.
Beaud, P., Johnson, S. L., Streun, A., Abela, R., Abramsohn, D., Grolimund, D., Krasniqi, F., Schmidt, T., Schlott, V. & Ingold, G. (2007). *Phys. Rev. Lett.* **99**, 174801.
Beaud, P., Johnson, S. L., Vorobeva, E., Staub, U., De Souza, R. A., Milne, C. J., Jia, Q. X. & Ingold, G. (2009). *Phys. Rev. Lett.* **103**, 155702.
Beaurepaire, E., Merle, J., Daunois, A. & Bigot, J. (1996). *Phys. Rev. Lett.* **76**, 4250–4253.
Bergerard, N. *et al.* (2014). *Nat. Commun.* **5**, 3466.
Boeglin, C., Beaurepaire, E., Halté, V., López-Flores, V., Stamm, C., Pontius, N., Dürr, H. A. & Bigot, J. Y. (2010). *Nature (London)*, **465**, 458–461.
Brzhezinskaya, M., Firsov, A., Holldack, K., Kachel, T., Mitzner, R., Pontius, N., Schmidt, J.-S., Sperling, M., Stamm, C., Föhlisch, A. & Erko, A. (2013). *J. Synchrotron Rad.* **20**, 522–530.
Chuang, Y. D. *et al.* (2013). *Phys. Rev. Lett.* **110**, 127404.
Chubar, O. & Elleaume, P. (1998). *Proceedings of the 1998 European Particle Accelerator Conference (EPAC 1998)*, pp. 1177–1179.
Eschenlohr, A., Battiato, M., Maldonado, P., Pontius, N., Kachel, T., Holldack, K., Mitzner, R., Föhlisch, A., Oppeneer, P. M. & Stamm, C. (2013). *Nat. Mater.* **12**, 332–336.
FERMI (2013). *FERMI*, http://www.elettra.trieste.it/FERMI/.
Fink, J., Schierle, E., Weschke, E. & Geck, J. (2013). *Rep. Prog. Phys.* **76**, 056502.
Gavrila, J., Godehusen, K., Weniger, C., Nibbering, E. T. J., Elsaesser, T., Eberhardt, W. & Wernet, P. (2009). *Appl. Phys. A*, **96**, 11–18.
Graves, C. E. *et al.* (2013). *Nat. Mater.* **12**, 293–298.
Holldack, K., Khan, S., Mitzner, R. & Quast, T. (2006). *Phys. Rev. Lett.* **96**, 054801.
Holldack, K., Pontius, N., Schierle, E., Kachel, T., Soltwisch, V., Mitzner, R., Quast, T., Springholz, G. & Weschke, E. (2010). *Appl. Phys. Lett.* **97**, 062502.
Ingold, G., Beaud, P., Johnson, S. L., Grolimund, D., Schlott, V., Schmidt, T. & Streun, A. (2007). *Synchrotron Radiat. News*, **20**(5), 35–39.
Jankowiak, A. & Wüstefeld, G. (2013). *Synchrotron Radiat. News*, **26**(3), 22–24.
Johnson, S. L. *et al.* (2012). *Phys. Rev. Lett.* **108**, 037203.
Jong, S. de *et al.* (2013). *Nat. Mater.* **12**, 882–886.
Khan, S. (2005). *Proceedings of the 2005 Particle Accelerator Conference (PAC 2005)*, Knoxville, TN, USA, pp. 1518–1520 and 590–594.
Khan, S., Holldack, K., Kachel, T., Mitzner, R. & Quast, T. (2006). *Phys. Rev. Lett.* **97**, 074801.
Kim, K. J. (1986). *X-ray Data Booklet*, PUB-490 Rev., pp. 4–7. Lawrence Berkeley Laboratory, USA.

Koopmanns, B. (2007). *Nat. Mater.* **6**, 715–716.
Lau, W. K. (2012). *Proceedings of the 2012 International Particle Accelerator Conference (IPAC 2012)*, New Orleans, LA, USA, pp. 1671–1673.
Lee, W. S. *et al.* (2012). *Nat. Commun.* **3**, 838.
Nadji, A. *et al.* (2004). *Proceedings of the 2004 European Particle Accelerator Conference (EPAC 2004)*, Lucerne, Switzerland, pp. 2332–2334.
Petersen, H., Jung, Hellwig, C., Peatman, W. B. & Gudat, W. (1995). *Rev. Sci. Instrum.* **66**, 1–14.
Pontius, N. *et al.* (2011). *Appl. Phys. Lett.* **98**, 182504.
Quast, T., Holldack, K., Khan, S. & Mitzner, R. (2008). *Proceedings of the 2008 European Particle Accelerator Conference (EPAC 2008)*, Genoa, Italy, pp. 172–174.
Radu, I. *et al.* (2014). In preparation.
Radu, I., Vahaplar, K., Stamm, C., Kachel, T., Pontius, N., Dürr, H. A., Ostler, T. A., Barker, J., Evans, R. F. L., Chantrell, R. W., Tsukamoto, A., Itoh, A., Kirilyuk, A., Rasing, T. & Kimel, A. V. (2011). *Nature (London)*, **472**, 205–208.
Sasaki, S., Miyata, K. & Takada, T. (1992). *Jpn. J. Appl. Phys.* **31**, L1794–L1796.
Sawhney, K. J. S., Senf, F., Scheer, M., Schäfers, F., Bahrdt, J., Gaupp, A. & Gudat, W. (1997). *Nucl. Instrum. Methods Phys. Res. A*, **390**, 395–402.
Scheer, M. (2012). *Proceedings of the International Computational Accelerator Physics Conference (ICAP 2012)*, Warnemünde, Germany, pp. 86–88.
Schierle, E., Weschke, E., Gottberg, A., Söllinger, W., Heiss, W. W., Springholz, G. & Kaindl, G. (2008). *Phys. Rev. Lett.* **101**, 267202.
Schoenlein, R. W., Chattopadhyay, S., Chong, H. H. W., Glover, T. E., Heimann, P. A., Shank, C. V., Zholents, A. A. & Zolotorev, M. S. (1996). *Science*, **274**, 236–238.
Schoenlein, R. W., Chattopadhyay, S., Chong, H. H. W., Glover, T. E., Heimann, P. A., Shank, C. V., Zholents, A. A. & Zolotorev, M. S. (2000). *Science*, **287**, 2237–2240.
Stamm, C., Kachel, T., Pontius, N., Mitzner, R., Quast, T., Holldack, K., Khan, S., Lupulescu, C., Aziz, E. F., Wietstruk, M., Dürr, H. A. & Eberhardt, W. (2007). *Nat. Mater.* **6**, 740–743.
Stamm, C., Pontius, N., Kachel, T., Wietstruk, M. & Dürr, H. A. (2010). *Phys. Rev. B*, **81**, 104425.
Streun, A. (2003). Report SLS-TME-TA-2003–0222. Swiss Light Source, Villigen, Switzerland.
Trabant, C. *et al.* (2013). *EPJ Web Conf.* **41**, 03014.
Turgut, E., La-o-Vorakiat, C., Shaw, J. M., Grychtol, P., Nembach, H. T., Rudolf, D., Adam, R., Aeschlimann, M., Schneider, C. M., Silva, T. J., Murnane, M. M., Kapteyn, H. C. & Mathias, S. (2013). *Phys. Rev. Lett.* **110**, 197201.
Weiss, M. R. *et al.* (2001). *Nucl. Instrum. Methods Phys. Res. A*, **467–468**, 449–452.
Wietstruk, M., Melnikov, A., Stamm, C., Kachel, T., Pontius, N., Sultan, M., Gahl, C., Weinelt, M., Dürr, H. A. & Bovensiepen, U. (2011). *Phys. Rev. Lett.* **106**, 127401.
Wilhein, T., Hambach, D., Niemann, B., Berglund, M., Rymell, L. & Hertz, H. M. (1997). *Appl. Phys. Lett.* **71**, 190–192.
Witte, S. & Eikema, S. E. (2012). *IEEE J. Sel. Top. Quantum Electron.* **18**, 296–306.
Yu, L. H. (1991). *Phys. Rev. A*, **44**, 5178–5193.
Yu, L. H. *et al.* (2011). *Proceedings of the 2011 Particle Accelerator Conference*, New York, NY, USA, pp. 2381–2383.
Zholents, A. A. & Holldack, K. (2006). *Proceedings of the Free Electron Laser Conference FEL 2006*, Berlin, Germany, pp. 725–728.
Zholents, A. A. & Zolotorev, M. S. (1996). *Phys. Rev. Lett.* **76**, 912–915.